polymers

MDPI

Article

Enhanced Performance of Chitosan via a Novel Quaternary Magnetic Nanocomposite Chitosan/Grafted Halloysitenanotubes@ZnγFe_3O_4 for Uptake of Cr (III), Fe (III), and Mn (II) from Wastewater

Mahmoud F. Mubarak [1,*], Ahmed H. Ragab [2], Rasha Hosny [3], Inas A. Ahmed [2], Hanan A. Ahmed [4], Salah M. El-Bahy [5] and Abeer El Shahawy [6,*]

1 Petroleum Application Department, Egyptian Petroleum Research Institute (EPRI), Nasr City, Cairo 11727, Egypt
2 Department of Chemistry, Faculty of Science, King Khalid University, Abha 62224, Saudi Arabia; ahrejab@kku.edu.sa (A.H.R.); eaahmed@kku.edu.sa (I.A.A.)
3 Production Department, Egyptian Petroleum Research Institute (EPRI), Nasr City, Cairo 11727, Egypt; rasha@epri.eg.org
4 Petrochemicals Department, Egyptian Petroleum Research Institute (EPRI), Nasr City, Cairo 11727, Egypt; Hanan@epri.eg.org
5 Department of Chemistry, Turabah University College, Taif University, P.O. Box 11099, Taif 21944, Saudi Arabia; s.elbahy@tu.edu.sa
6 Department of Civil Engineering, Faculty of Engineering, Suez Canal University, Ismailia 41522, Egypt
* Correspondence: mahmoud@epri.eg.org (M.F.M.); abeer_shahawi@eng.suez.edu.eg (A.E.S.)

check for updates

Citation: Mubarak, M.F.; Ragab, A.H.; Hosny, R.; Ahmed, I.A.; Ahmed, H.A.; El-Bahy, S.M.; El Shahawy, A. Enhanced Performance of Chitosan via a Novel Quaternary Magnetic Nanocomposite Chitosan/Grafted Halloysitenanotubes@ZnγFe_3O_4 for Uptake of Cr (III), Fe (III), and Mn (II) from Wastewater. *Polymers* **2021**, *13*, 2714. https://doi.org/10.3390/polym13162714

Academic Editors: Keiko Shirai, Maribel Plascencia-Jatomea and Neith Aracely Pacheco López

Received: 17 July 2021
Accepted: 9 August 2021
Published: 13 August 2021

Publisher's Note: MDPI stays neutral with regard to jurisdictional claims in published maps and institutional affiliations.

Abstract: A novel chitosan/grafted halloysitenanotubes@Znγmagnetite quaternary nanocomposite (Ch/g-HNTs@ZnγM) was fabricated using the chemical co-precipitation method to remove the ions of Cr (III), Fe (III), and Mn (II) from wastewater. The characteristics of the synthesized Ch/g-HNTs@ZnγM quaternary nanocomposite were investigated using FTIR, SEM, XRD, GPC, TGA, TEM, and surface zeta potential. The characterization analysis proved that the mentioned nanocomposite structure contains multiple functional groups with variable efficiencies. Additionally, they proved the existence of magnetic iron in the nanocomposite internal structure with the clarity of presentation of gaps and holes of high electron density on its surface. The results showed that the pH and time to reach an equilibrium system for all the studied metal ions were obtained at 9.0 and 60 min, respectively. The synthesized Ch/g-HNTs@ZnγM nanocomposite exhibited maximum adsorption removal of 95.2%, 99.06%, and 87.1% for Cr (III), Fe (III), and Mn (II) ions, respectively. The pseudo-second-order kinetic model and, for isotherm, the Langmuir model were best fitted with the experimental data. The thermodynamic parameters indicated the exothermic and spontaneous nature of the adsorption reaction as proven by the ΔH° and ΔG° values. Additionally, chemical adsorption by the coordination bond is supposed as the main mechanism of adsorption of the mentioned metal ions on the nanocomposite. Finally, Ch/g-HNTs@ZnγM displays prospected advantages, such as a low-expense adsorbent, high efficiency and availability, and an eco-friendly source, that will reduce the environmental load via an environmentally friendly method.

Keywords: chitosan; halloysite; quaternary magnetic nanocomposite; heavy metals; wastewater treatment

1. Introduction

Among the various sources of water pollution with heavy metals, the rapid increase in industrialization is causing many environmental problems day by day [1]. Water pollution has reached a point of threatening human and aquatic life. Heavy metals accumulate in living organisms because of their toxicity and non-biodegradability [2,3]. Therefore, they can cause a lot of acute and chronic diseases. The treatment of industrial wastewater including

heavy metals is becoming an important subject for improving water quality. Cd (II), Cr (III), Cu (II), Fe (III), Mn (II), and Ni (II) are considered as some of the most toxic metals for living organisms when their concentration exceeds the required limits [4]. Increased chromium exposure leads to cancer, asthma, and diarrhea. Physiological deficiency is caused by liver disease, kidney complications, and a brain defect [5,6]. The presence of iron in wastewater above the tolerable level can cause intestinal damage and respiratory tract irritation [7]. Additionally, the contamination of water with Mn (II)/Fe (III) ions leads to poor water taste, odour, colour, and turbidity; Mn (II)/Fe (III) water pollution also causes many chronic diseases [8].

Chemical precipitation, flotation, reverse osmosis, ultrafiltration, electrochemical precipitation, ion exchange, chemical oxidation, adsorption, and other conventional treatment methods are generally used to remove heavy metals from wastewater [9,10]. Most of the mentioned techniques have ingrained restrictions, such as low efficiency, the generation of significant quantities of sludge, and costly disposal, except adsorption [9]. Adsorption is the most preferred among the mentioned treatment technologies for extracting heavy metals from wastewater because of its efficiency [10]. It provides design flexibility, and the treated effluents are of high quality, are reversible, and absorbent materials can be regenerated [11,12]. Among the substances used to remove metal ions from contaminated water by adsorption are alumina, silica, activated carbon, graphene oxide, manganese oxides, ferric oxide nanoparticles, polyaniline, titanium oxides, and zinc oxide [13–15]. Lately, scientists have focused on preparing new multifunctional adsorbents with low costs and ease of use [16,17]. These adsorbents may be composed of synthetic or natural substrates, such as industrial byproducts, clays, biosorbents, and modified biosorbents [18,19]. Among these substrates, chitosan (natural biopolymers) [20] is considered an effective adsorbent for removing heavy metals [21] because it is a polysaccharide with the functional groups -OH and -NH_2, is hydrophilic and biodegradable, and is easy to derive because of its ability to form chelates with the heavy metals [22,23]. However, it is known for its mechanical weakness, [23,24] its ability to dissolve in an acidic medium, and its capability of leaching carbohydrates if utilized in its raw structure [25]. Therefore, several adsorbents, including "magnetic" nanoparticles and chitosan, have been prepared and have shown their excellent efficiency for heavy metal removal from wastewater [26,27]. Magnetic adsorbents are considered alternative adsorbents because of their fascinating properties, i.e., high adsorption performance and magnetic characteristics, facilitating their separation by applying an external magnet [28,29]. Magnetic gamma iron oxide (γ ferric oxide Fe_2O_3) is one of the iron oxides which has a high magnetic field compared to the other three iron oxides, i.e., Fe_3O_4 (iron (II, III) oxide) and FeO (iron (II) oxide) [30,31]. When γ Fe_2O_3 (ferric oxide) is embedded with natural polymers, it gives a high potential nanocomposite that can be used in many fields such as medicine and water treatment due to its high ability to adsorb organic and inorganic pollutants [32].

Based on the above-mentioned concerns, this paper focused on searching for low cost-effective adsorbents and eco-friendly methods to treat wastewater from inorganic effluent (heavy metals) [33]. Herein, chitosan extract was abstracted for shrimps [34]. A novel adsorbent quaternary nanocomposite, chitosan/grafted halloysitenanotubes@Znγmagnetite (Ch/g-HNTs@ZnM), was synthesized via the ultrasonic-assisted adhesion technique to adsorb the Cr (III), Fe (III), and Mn (II) from wastewater. The characteristics of chitin (chitosan extract), halloysite, Zn@Fe_3O_4, and the synthesized Ch/g-HNTs@ZnγM quaternary nanocomposite were revealed by several techniques, including FTIR, SEM, XRD, GPC, TGA, TEM, and surface zeta potential. Batch processes with the synthesized Ch/g-HNTs@ZnγM were investigated. Generally, adsorption via the continuous column process is the most promising method for the future wastewater treatment implementations of existing adsorbents. The various factors affecting the metal ion removal efficacy on the Ch/g-HNTs@ZnγM adsorbent were studied. The effects of solution pH, metal ions' initial concentration, temperature, quaternary adsorbent dosage, and contact time were investi-

gated for batch adsorption. Additionally, nonlinear regression was designed for various kinetic and equilibrium models to evaluate the adsorption data.

2. Experiments

2.1. Materials

The authors have utilized sodium hydroxide (NaOH) (99.99%, Sigma Aldrich, Munich, Germany), hydrochloric acid (HCl), calcium carbonate ($CaCO_3$), potassium hydroxide (KOH), distilled water, deionized (DI) water, acetic acid, an aqueous solution of sodium dodecyl sulfate (SDS), Ethylenediaminetetraacetic acid (EDTA), ferric nitrate $Fe(NO_3)_3$, zinc nitrate $Zn(NO_3)_2$, and halloysite solution to complete the following experiments.

2.2. Extraction of Chitosan

Fresh shrimp shells were locally obtained from an Egyptian market in Cairo. After removing their legs and heads, the shells were well rinsed repeatedly with tap water, followed by their drying at 70 °C and grinding into fine powder [35].

Chitosan (Ch) was then extracted from the shrimp shell powder according to Hosny et al., 2014 [20]. First, the deproteinization process was performed by adding 0.1 N NaOH solution to the shrimp shells with continuous stirring for two days to remove proteins, filtration of the produced solution at 25 °C, and washing the filter with distilled water to the pH of 7. Second, the demineralization process was carried out by stirring the resulting filter for 8 continuous days in 200 mL of a 3–5% hydrochloric acid solution, then filtering and washing to eliminate the minerals and obtain pure chitin. Finally, the deacetylation was achieved by hydrolyzing the produced chitin in 50% NaOH and stirring for 4 h at a fixed temperature of 40 or 90 °C, followed by washing the filter with water at 50 °C while stirring for 5 h to produce pure chitosan at a pH of 7. The mentioned steps for pure chitosan extraction from shrimp shells are depicted in Figure 1.

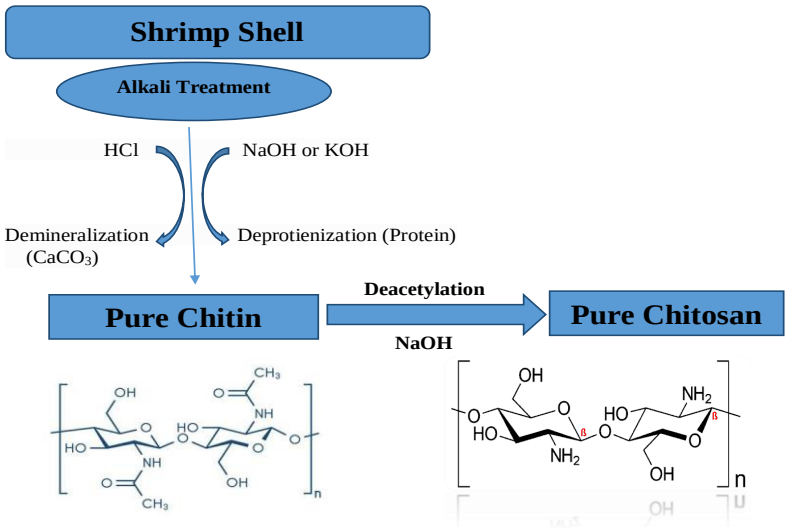

Figure 1. Simplified chemical extraction method of chitin and chitosan from shrimp shells.

2.3. Synthesis of Halloysite Nanotubes/ZnγFe_3O_4 Core/Shell (HNPs/ZnγM)

Halloysite suspension solution was prepared by vigorously stirring 5.0 g halloysite in a 200 mL aqueous solution. Then, the halloysite solution was impregnated by ZnγFe_3O_4 particles to produce (HNTs/ZnγM) core/shell using the chemical precipitation method. In detail, zinc/iron precursors solution consisting of ferric nitrate $Fe(NO_3)_3$ and zinc nitrate $Zn(NO_3)_2$ was added dropwise to the 1% halloysite suspension solution. The $Fe(NO_3)_3$:$(Zn(NO_3)_2)$ stoichiometric ratio was 4:1 in the solution. The final black (HNTs/ZnγM) suspension was rinsed repeatedly with re-distilled water, dried at 50 °C for 24 h and at different temper-

atures (100 °C to ~500 °C, the interval was 50 °C), and calcined for 2 h in the air with consideration of a 1 °C/min heating rate.

2.4. Synthesis of a Novel Chitosan/Grafted Halloysite@ZnγFe_3O_4 Tetra-Nanocomposite (Ch/g-HA@ZnγM)

The ultrasonic-assisted adhesion method was used to synthesize the Chitosan/grafted Halloysite@ZnγFe_3O_4 tetra-nanocomposite (Ch/g-HNTs@ZnγM) because it diminishes the time of crystallization and forms more consistent nuclei. Briefly, in the first step, the ultrasonic dispersion method was applied for 30 min at 25 °C on a mixture solution containing 0.5 g Fe_3O_4-NH_2 and 0.862 g (3 mmoL) $Zn(NO_3)_2{\cdot}6H_2O$, and dissolved in 30 mL of ethanol and containing $Zn(NO_3)_2{\cdot}6H_2O$. 0.862 g (3 mmoL). In this step, the magnetic Fe_3O_4 in its nanoscale was added to adhere to the surfaces of Metal–Organic Frameworks (MOFs) precursor solution ($Zn(NO_3)_2{\cdot}6H_2O$) to form MMOFs (ZnγFe_3O_4). Secondly, the same technique was applied on another mixture containing 1.50 g (9 mmoL) chitosan and 0.1 g PVP soluble in 30 mL of ethanol. Then, the mixture solution of the second step was stepwise added to the first one and dispersed together by ultrasonic for 1 h at 25 °C, then aged at 60 °C for 3 h. Lastly, the chitosan/grafted halloysitenanotubes@ZnγFe_3O_4 tetra-nanocomposite was produced by washing the mixture solution with anhydrous ethanol and deionized water drying by a vacuum pump at 50 °C for 24 h. The expected schematic diagram of Ch/g-HNTs@ZnγM synthesis is shown in Figures 2 and 3.

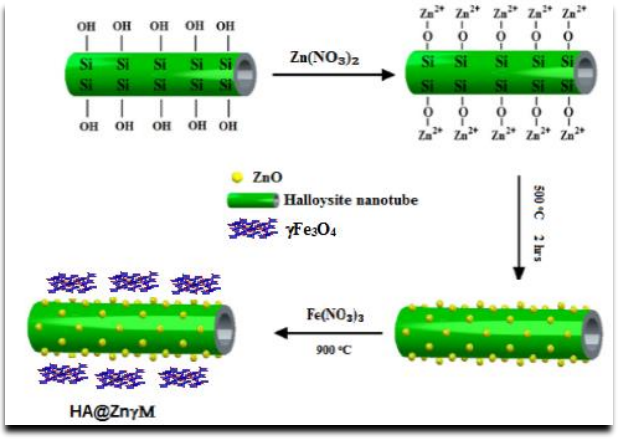

Figure 2. Scheme of the synthesis of halloysite/ZnγFe_3O_4 core/shell (HNTS/ZnγM).

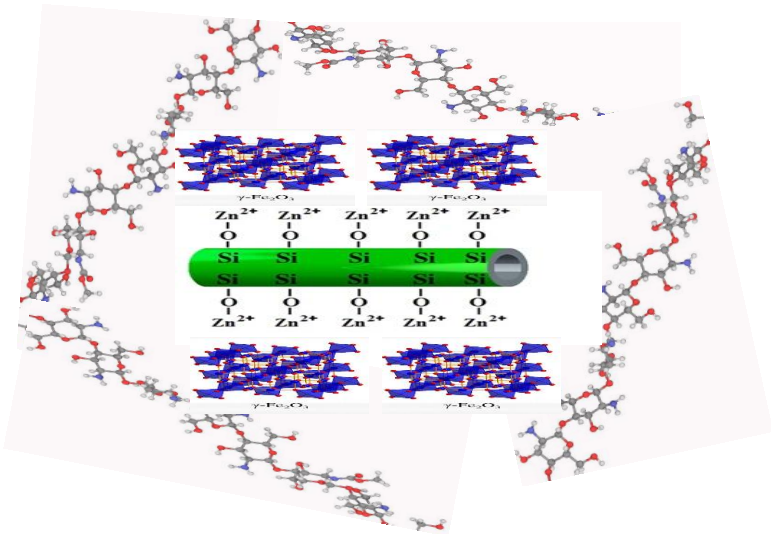

Figure 3. Scheme of the predicted shape of the synthesized quaternary magnetic nanocomposite Ch/g-HNTs@ZnγM.

2.5. Characterization of Materials

The synthesized materials were analyzed with the ATR FTIR spectra (SHIMADZU, IRAffinity-1S, Surgut, Russia) over the wavenumber 4000–400 cm^{-1}. The prepared chitosan molecular weight and thermogravimetric analysis (TGA) of chitosan and Ch/g-HNTs@ZnγM nanocomposite were determined by the GPC analysis. A supremamax 3000 column (Mainz, Germany) was used. At the same time, the TGA-50 Shimadzu instrument was under air at a heating rate of 10 °C min^{-1} from 25 °C to 600 °C. The synthesized materials' surface morphologies were investigated at 120 kV by a Scanning Electron Microscope (SEM, Quanta 450 FEG, FEI Company, North Brabant, Netherlands). XRD diffraction analysis was performed with PAN alytical–Empyrean using Cu Kα radiation (λ = 0.15406 nm, 40 mA, 45 kV, step size (°2Th.) 0.0260). TEM with Model JEM-200CX (JEOL 2100, JEOL, Tokyo, Japan), operated at 200 kV, was used to investigate the morphology of the halloysite and magnetic halloysite samples. An important parameter is the pHpzc of the adsorbents characterized by the Zeta sizer Nano (Malvern, UK), which defines the pH at which the adsorbent surface has net electrical neutrality. The wet Ch/g-HNTs@ZnγM beads surface charge was examined using the method described elsewhere to determine the point of zero charges for the adsorbent. Usually, 0.1 g of the wet synthesized composite was mixed with 40 mL of H_2O. Each solution's pH was changed from 3 to 12 using (0.1 M) H_2SO_4 or NaOH. Then, the suspensions were shaken at 250 rpm for 48 h before pH equilibrium was reached. The pHpzc was the point where the plot of pH (pH = $pH_f pH_i$) (*Y*-axis) vs. pH_i intersected (*X*-axis).

2.6. Adsorption Experiments

The batch adsorption studies were carried out in beakers with 25 mL of the studied heavy metals solutions of a certain concentration (15 mg/L) with a specific Ch/g-HNTs@ZnγM adsorbent dosage. Shaking of the solution was performed at a particular rate of 50 rpm for various contact times (10–260 min). Processing factors including initial metals concentrations, PH, temperatures, Ch/g-HNTs@ZnγM tetra-nanocomposite dosage, and time intervals were explored and optimized for studying the maximum heavy metal removal. At the end of shaking, the absorbance values of the studied heavy metals residual were measured at a wavelength of 250–664 nm by a UV-Vis spectrophotometer (JENWAY 6715, Shimadzu, Columbia, MD, USA). Each experiment was repeated in triplicate, and the average values were utilized for analyzing the adsorption data. Various adsorption temperatures in the range of 25–55 °C were examined at a constant Ch/g-HNTs@ZnγM tetra-nanocomposite dosage and heavy metals concentrations to study the adsorption thermodynamics. The studied heavy metal removal percentage (*R*%) was determined by Equation (1) [36].

$$R\,\% = \frac{(C_0 - C_e)}{C_o} \times 100 \quad (1)$$

C_o is the metal ions' initial concentrations (mg/L), and C_e is the remaining metal ions concentrations after treatment (mg/L).

3. Results and Discussion

3.1. Characterization of Materials

3.1.1. Physical and Chemical Characterization of Prepared Chitin and Chitosan

Chitin and chitosan are bio-macromolecules (natural polymers). Their various characteristics, i.e., the prepared chitin and chitosan, are estimated based on FTIR spectra, X-ray diffraction analysis, gel permeation chromatography (GPC), thermal analysis, and a scanning electron microscope (SEM).

3.1.2. Fourier Transform Infrared (FTIR) Spectra

The prepared chitin chemical bonds are investigated by FTIR spectra, as depicted in Figure 4. This spectrum shows a band at 1659 cm^{-1} and an intensive band at 1319 cm^{-1}, respectively, correlated to the stretching vibration of CN superimposed to the C=O group

linked by a hydrogen bond with the –OH group, CH_3 group asymmetrical deformation or rocking. The non-existence of a band at 1540 cm^{-1} demonstrated that the successive chitin treatment was strong enough to eliminate all the proteins; thereby, pure chitin was obtained.

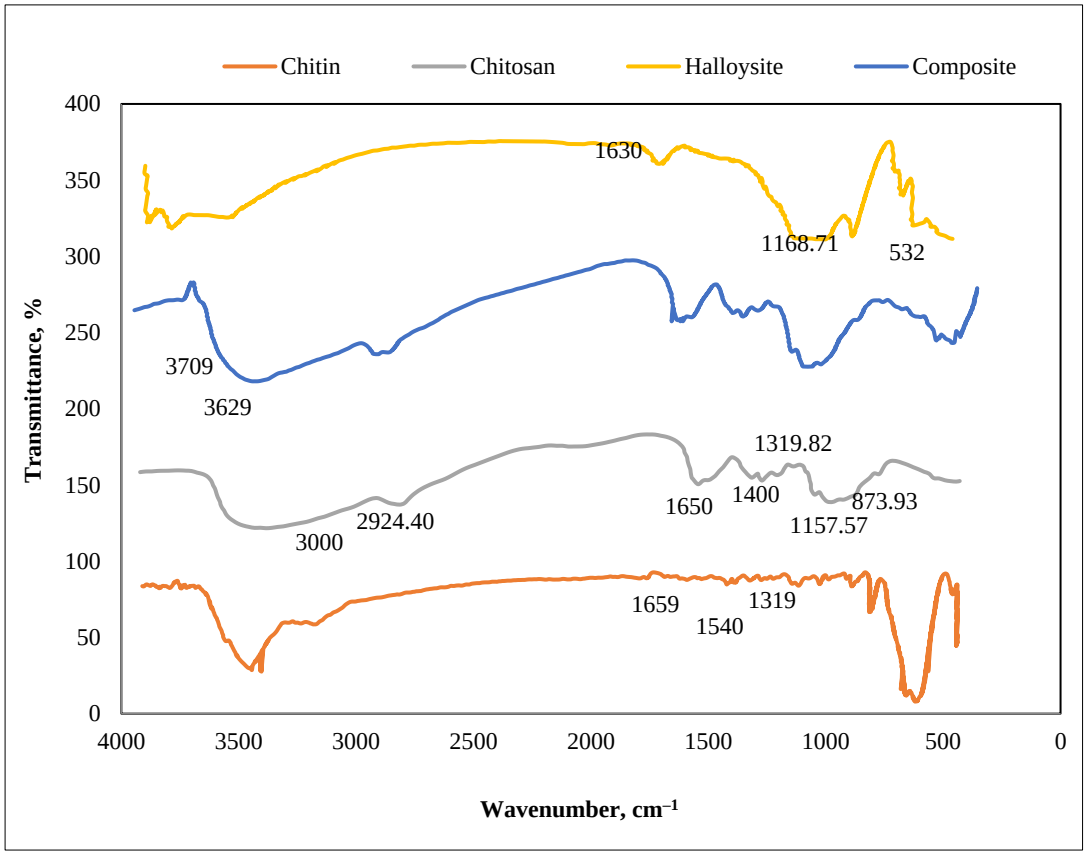

Figure 4. FTIR spectra of chitin, chitosan, halloysite, and composite.

Figure 4 also represents the FTIR spectrum of chitosan. In general, chitosan shows bands at 1400–1650 cm^{-1} (C=O bonds), as illustrated by Chatterjee S. et al., 1994 [37]. The broad FTIR bands that appeared in the range of 3000–3500 cm^{-1} are correlated to the stretching vibration of O–H. The characteristic absorption bands of chitosan which appeared at 1319.82 cm^{-1}, 2924.40 cm^{-1}, and at 1555.69 cm^{-1} and 3263.72 cm^{-1} are correlated to C-H and amino vibrations groups. This spectrum also exhibits two bands at 873.93 cm^{-1}, and 1157.57 cm^{-1} that characterize chitosan's saccharide and polysaccharide structure.

For the halloysite sample (Figure 4), its spectrum emphasizes FTIR bands at 3709 cm^{-1} and 3629 cm^{-1}, respectively, due to the inner surface -OH groups and the inner –OH groups stretching vibrations.

For the Ch/g-HNTs@ZnγM magnetic tetra-nanocomposite sample (Figure 4), the appearance of a new band at 532 cm^{-1} reports the Fe–O stretching mode, indicating the existence of Fe_3O_4 functional groups. The FTIR band recorded at 1168.71 cm^{-1} was moved to 1630 cm^{-1} with low intensity compared to the chitosan spectrum. The nanocomposite spectrum, the spectrum of the other samples, and the formation of Ch/g-HNTs@ZnγM magnetic tetra-nanocomposites through the N=C groups and the -OH links with halloysite were verified. The Fe-O absorption band of Fe_3O_4 appeared at a lower wavenumber than the ZnγFe3O4 sample., possibly because of the electrostatic strength between the surface and the halloysite of ZnγFe_3O_4. A Fe-O absorption band was still in the magnetic halloysite chitosan, which suggested using an electrostatic activity to cover the ZnγFe_3O_4 particles of halloysite in the magnetic composite.

3.1.3. X-ray Diffraction (XRD)

The phase structure of chitin and chitosan powders was obtained through X-ray diffraction (XRD) measurements. The XRD diffraction peaks shown in Figure 5 confirm the successful chitin conversion into chitosan. At 2θ = 9.24° and 19.2°, two distinct sharp peaks of chitin were observed, which gradually decreased and became broad after conversion, suggesting that chitosan was fully extracted from chitin. The differences between them can be related to the change of the amorphous structure of the prepared chitin into a crystalline phase of chitosan, evidencing the complete and successful preparation of chitosan as described in agreement with Zhang et al. 2005 [38].

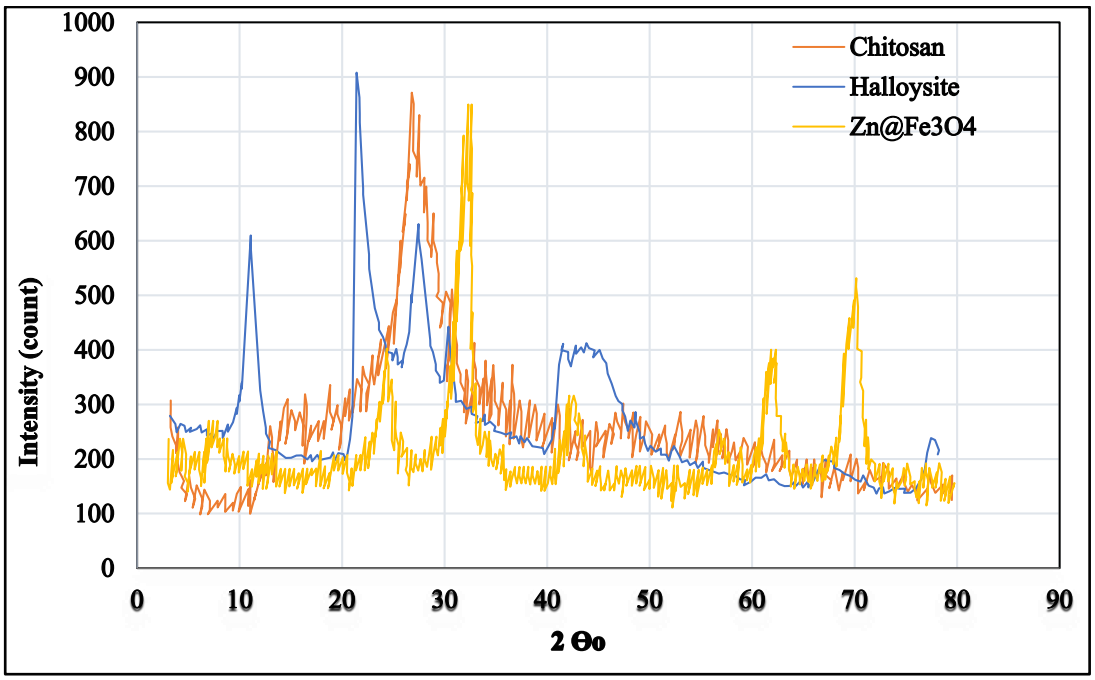

Figure 5. X-ray diffractions (XRD) for chitosan, halloysite, Zn@Fe_3O_4, and composite.

The XRD patterns of ZnγFe_3O_4 nanoparticles are shown in Figure 5. In the 2θ range of 19.20°, 24.14°, 31.86°, 42.50°, 56.3°, and 61.787°, broad reflections exist due to the (111), (210), (220), (400), (511), and (440) diffraction planes of ZnγFe_3O_4. Additionally, the halloysite patterns display their characteristic reflections at the 2θ range of 11.08°, 21.42°, 27.45°, and 30.37° [39,40].

Magnetic tetra-nanocomposite patterns display characteristic peaks at 2θ = 9°, 30°, 32°, 35.5°, and 70.0 that can be indexed in the diffraction planes of (001), (311), (400), (422), (511). At the same time, it is worth noting that the diffraction peaks of chitosan disappeared into the XRD pattern of the magnetic composite caused by the presence in the chitosan matrix of ZnγFe_3O_4 nanoparticles with halloysite. Thus, ZnγFe_3O_4 magnetic nanoparticles retained their magnetic properties.

3.1.4. Thermal Analysis

The thermal decomposition of chitosan (TGA curve) is shown in Figure 6. In this curve, there are two decomposition stages. The first one begins at 60 °C, with a 6% weight loss due to the water loss. The second one nearly starts at 150 °C with a weight loss of about 47%. It stabilizes at 350 °C, and eventually reaches a total weight loss of 59% at about 500 °C, due to the decomposition of chitosan.

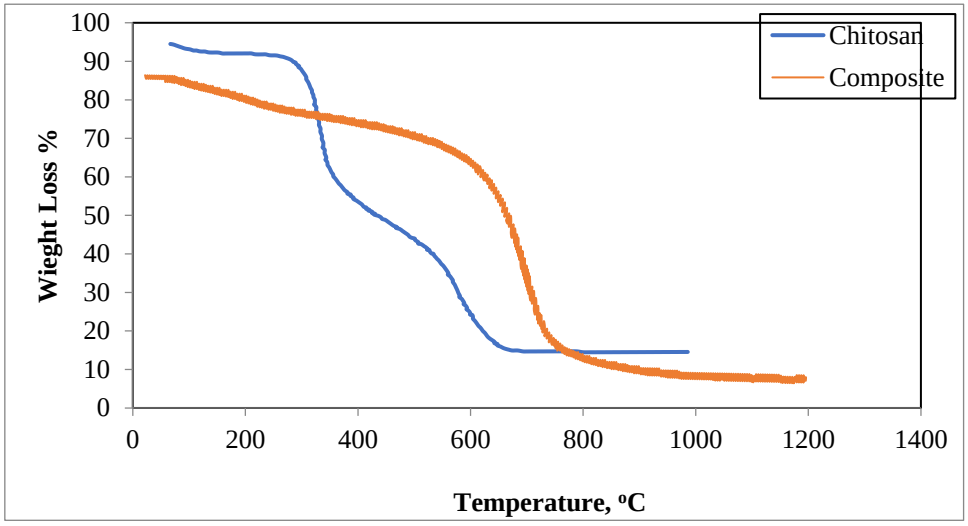

Figure 6. Thermogravimetric analysis (TGA) for chitosan and composite.

Figure 6 also shows the TGA curve of the magnetic tetra-nanocomposite where the adsorbed water at the surface induces a weight loss at 160 °C. A substantial loss of weight can also occur between 150 °C and 650 °C. A loss of mass by decomposition occurs in the TGA curve, which contains the halloysite and $Zn\gamma Fe_3O_4$, caused by the combustion of these fillers gradually to 650 °C.

3.1.5. Gel Permeation Chromatography (GPC)

The average molecular weights of chitosan are determined by the gel permeation chromatography (GPC) using water after 60 min and 120 min, as represented in Tables 1 and 2. The weight-average molecular weights (Mw) were 86,380 and 110,534, while the number-average molecular weights (Mn) were 50,015 and 51,518 at 60 min and 120 min, respectively.

Table 1. GPC for chitosan sample after 60 min.

Retention Time	M_n	M_w	M_p	M_z	M_{z+1}	Polydispersity
27.220	50,015	86,380	50,493	144,904	208,744	1.727065

Table 2. GPC for chitosan sample after 120 min.

Retention Time	M_n	M_w	M_p	M_z	M_{z+1}	Polydispersity
26.112	51,518	110,534	90,177	193,865	260,533	2.145541

3.1.6. Scanning Electron Microscope (SEM)

SEM was used to characterize the surface morphology of chitin and chitosan. Figure 7 shows the SEM images of chitosan and chitin. Chitin powder exhibits almost a smooth surface (Figure 7A), while the chitosan powder exhibits a rough surface (Figure 7B). It can be observed that chitosan has an irregular diameter in the range of 14.6–37.6 µm with cracks and pores on its surface, and the number of pores increased significantly, as illustrated in Hosny, 2014 [41]. Consequently, it can be concluded that chitosan has pores and cracks in its surface more than chitin; this gives chitosan a high ability to adsorb heavy metals more than chitin.

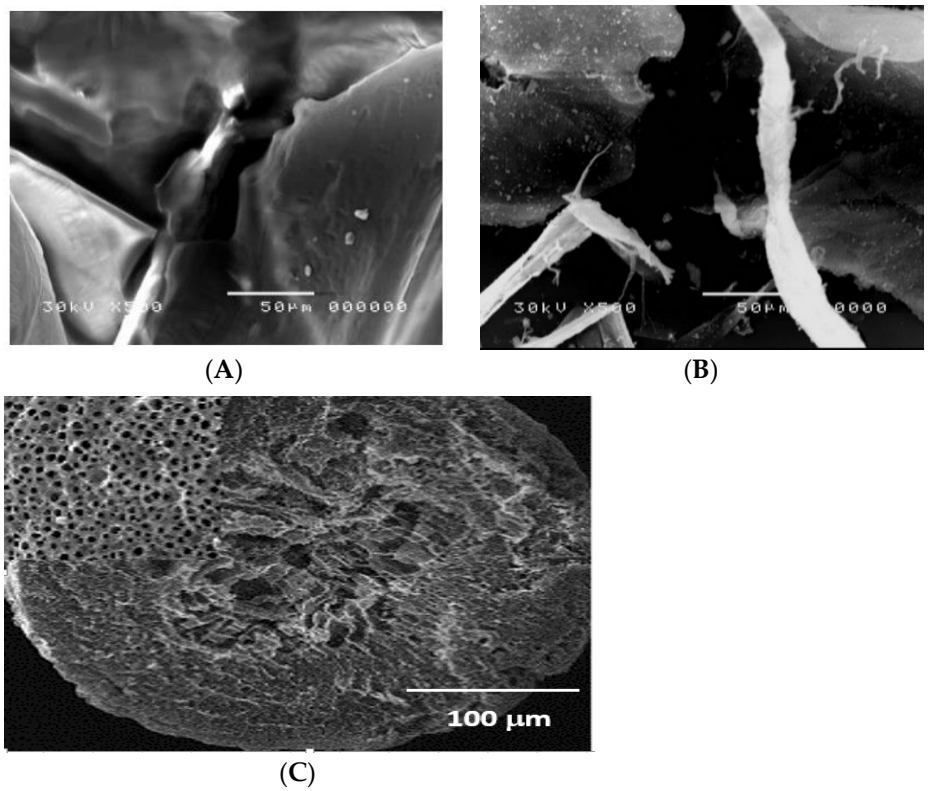

Figure 7. SEM micrographs for (**A**) chitin, (**B**) chitosan, and (**C**) Ch/g-HNTs@ZnγM composite.

SEM images of the magnetic composite were evaluated to describe the size and morphology of these synthesized constructions. According to exact research, the SEM histogram of the magnetic composite is shown in Figure 7. Following the accuracy of the findings, we can see that the magnetic composite was distinguished by a uniform, virtually similar morphology with sphere shapes. It can be noticed that the synthetic nanocomposite filler ZnγFe_3O_4/halloysite has a core–shell structure. The average dimensions of the nanocomposite ZnγFe_3O_4/halloysite were calculated in a magnetic composite body. The dimensions were between 45 and 62 nm.

3.1.7. TEM

Transmission electron microscopy (TEM) was used for the morphological study of loaded and discharged ZnγFe_3O_4 halloysite tubes. Halloysite tubes were morphologically tubular and held the same after grafting, as shown in Figure 8. Halloysite tubes were found to have a lumen diameter between 50 nm and 65 nm, while possessing a length between 100 and 170 nm. The TEM images of the loaded halloysite $ZnFe_3O_4$ have a morphology, validated by TEM analysis, random and free of any defects (i.e., beads, globules, and undefined form). It can be concluded that the ZnγFe_3O_4-loaded halloysite has similar morphological characteristics (Figure 8). ZnγFe_3O_4 was filled with average diameters of 150 ± 45 nm.

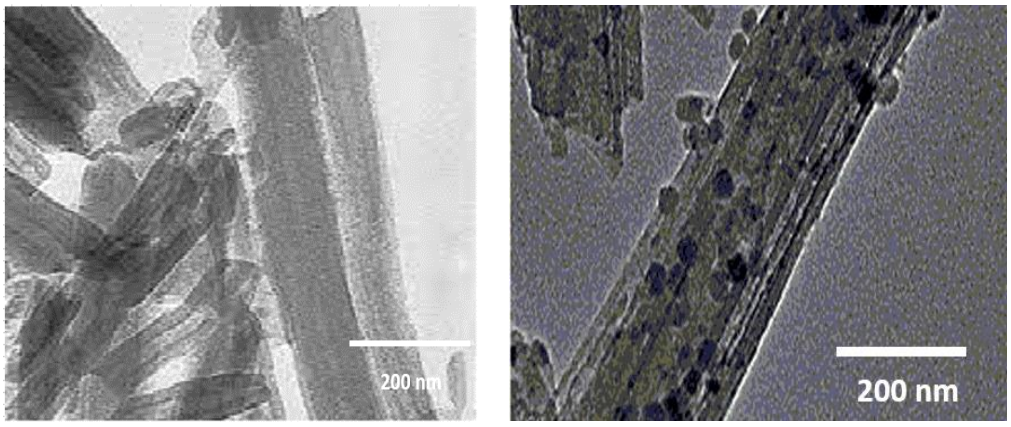

(**a**) (**b**)

Figure 8. TEM of (**a**) halloysite and (**b**) magnetic halloysite.

3.1.8. Ch/g-HNTs@ZnγM Zero Charge Point (pHpzc)

An important parameter is the point of zero charge (pHpzc) of the adsorbents since it determines the pH at which the adsorbents surfaces have net electrical neutrality [16]. The technique of pH drift was applied to define the pHpzc of the Ch/g-HNTs@ZnγM tetra-nanocomposite, as shown in Figure 9. The results estimated that the PZC for the Ch/g-HNTs@ZnγM composite was pH of 10.9, indicating that the Ch/g-HNTs@ZnγM particles acquire a positive charge below this pH, while, above this pH, the particles acquire a negative charge.

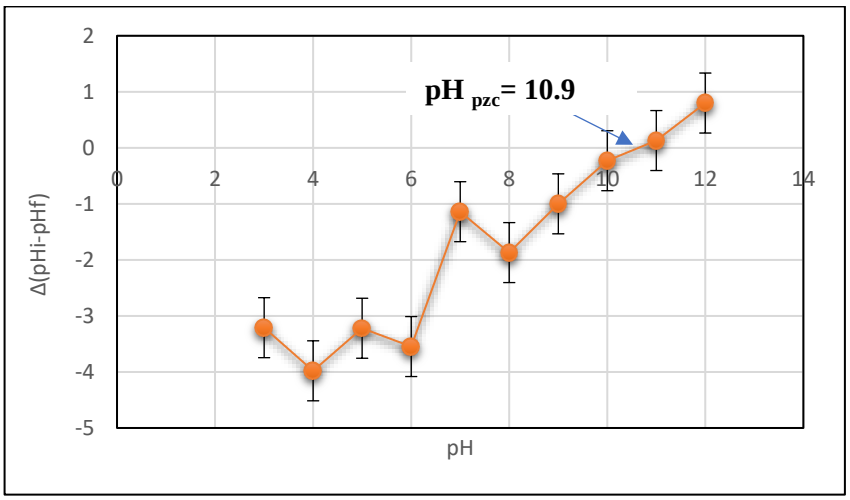

Figure 9. Point of zero charge (pH_{PZC}) of the Ch/g-HNTs@ZnγM, determined by the pH drift technique.

3.1.9. N_2 Adsorption-Desorption

The nitrogen sorption measurements were performed to investigate the textural characteristics of resultant Ch/g-HNTs@ZnγM nanocomposites. The nitrogen isotherms in Figure 10 resulted in a type IV shape with an H_2 hysteresis loop in the range of 0.3–0.98 relative pressure. These results suggest that the Ch/g-HNTs@ZnγM nanocomposites are characterized by mesoporous structures with pore sizes of 20–30 nm. These vicissitudes in hysteresis and pore size distribution may be ascribed to the role played by chitosan in tailoring the pore structure of the nanocomposites, which stems from integrating two-dimensional (chitosan sheets) and zero-dimensional (Zn γFe3O4 NPs) structures into a single material.

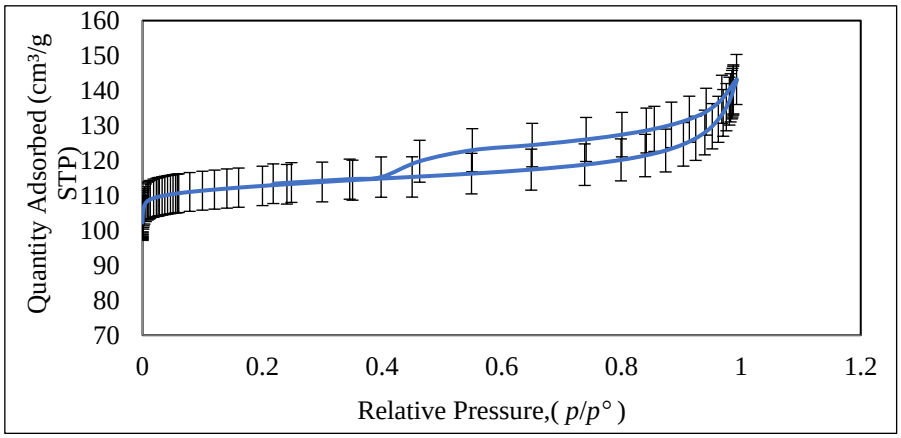

Figure 10. Nitrogen adsorption–desorption isotherms of Ch/g-HNTs@ZnγM nanocomposites.

3.2. Effect of Parameters on Ions Removal

3.2.1. Effect of Concentrations, at Constant Temperature = 30 °C and pH = 9

The effect of varying the mentioned ion concentrations (20 mg/L to 60 mg/L) was studied using the adsorbent Ch/g-HNTs@ZnγM while holding the other parameters such as pH = 9 and temperature = 30 °C. Figure 11 represents the concentrations of the ions versus the percentage of removal. This figure reveals that the Fe (III) removal % was increased by increasing the ion concentrations until 40 mg/L, corresponding to 99.06% removal efficiency then decreasing to 93.3% at 60 mg/L. The high ability of Ch/g-HNTs@ZnγM to adsorb Fe (III) may be due to that chitosan is a versatile polymer and has reactive (NH_2 and-OH) groups on its backbone, which leads to a variety of applications and characteristics [42,43]. On the contrary, the adsorption of Cr (III) and Mn (II) by Ch/g-HNTs@ZnγM decreased by increasing the ion concentrations and reached the maximum removal of 95.2% and 87.1% at 20 mg/L. It is clear that the Ch/g-HNTs@ZnγM is slightly susceptible to the adsorption of Cr (III) and Mn (II) even with increasing their concentrations at fixed pH and temperature.

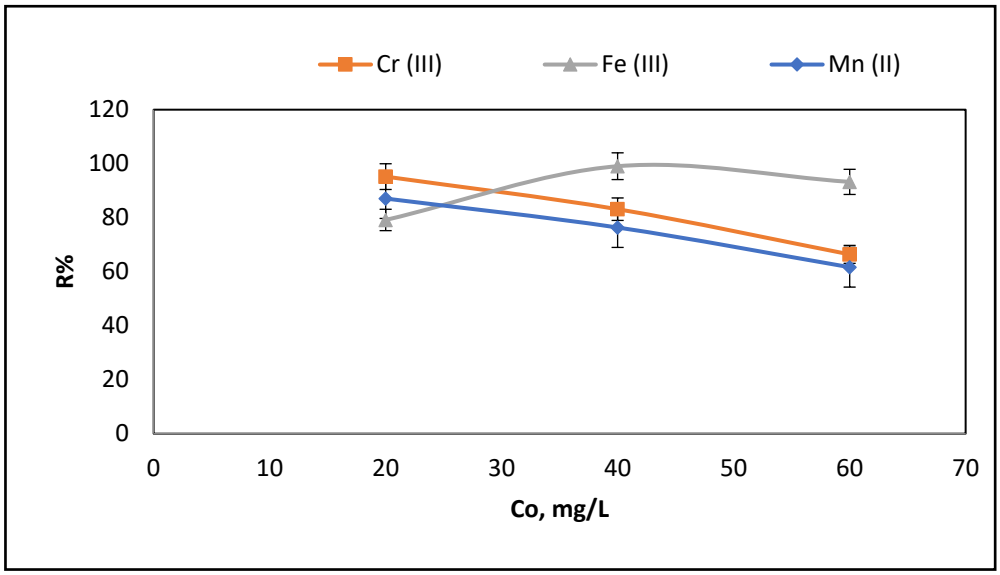

Figure 11. Effect of initial metals concentrations on the Cr (III), Fe (III) and Mn (II) removal onto Ch/g-HNTs@ZnγM at 30 °C and pH 9.

3.2.2. Effect of pH at Constant Concentration = 20 mg/L and Temperature = 30 °C

One of the variables which influences the adsorption efficiency is solution pH since it defines the adsorbent surface charge, the ionization extent, and the adsorbent specia-

tion [11]. The adsorption effect of Cr (III), Fe (III), and Mn (II) ions onto Ch/g-HNTs@ZnγM was studied in the pH range of 3.0–10.0 while maintaining the initial concentrations of the mentioned ions at 20 mg/L and the adsorbent Ch/g-HNTs@ZnγM dose at 2 g in 100 mL of solution at 30 °C. The effect of pH versus the percentage of the removed metal ions is shown in Figure 12. The results revealed that the removal percentage of the Cr (III) ion increased significantly with increasing the solution pH, as the highest removal percentage was 96% at the pH of 9, which could be related to the change in the surface charge distribution that significantly impacts metal ion removal. The adsorbent surface becomes positively charged at a low pH, pH = 2, because of H^+ ion adsorption from the acidic medium, enhancing the adsorption of the negative loaded Cr (III) ions, which presents in the form of $HCrO_4^-$ at that pH. The iron (III) ions adsorption potential decreased with increasing the solution pH. As a result, increasing the adsorption ratio of metal ions was observed in the order of Cr (III) > Fe (III) > Mn (II).

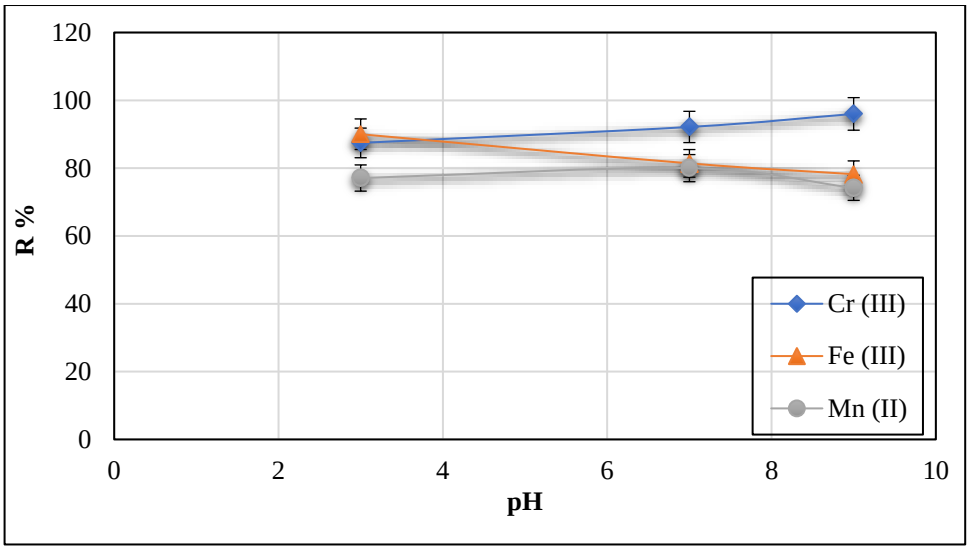

Figure 12. Effect of solution pH on Cr (III), Fe (III), and Mn (II) adsorption onto Ch/g-HNTs@ZnγM adsorbent at 30 °C and concentration of 20 mg/L.

3.2.3. Effect of Temperatures at C_o = 20 mg/L and pH = 9

The operating temperatures at which heavy metal adsorption processes are carried out is a significant factor that influences adsorption ability and behaviour. Figure 13 shows the effect of adsorption temperature on Cr (III), Fe (III), and Mn (II) adsorption using Ch/g-HNTs@ZnγM as an adsorbent at a concentration of 20 mg/L, a pH of 9, and temperatures ranging from 300 to 350 K.

According to Figure 13 results, the adsorption removal rate decreases with the adsorption temperature increase, indicating the exothermic nature of the adsorption process, which agrees with the enthalpy change (ΔH) negative values. Consequently, at the temperature of 303.15 K (30 °C), the maximum removal percentages understudied occurred as 95.2%, 88.15%, and 87% for Cr (III), Fe (III), and Mn (II), respectively. The decrease in process efficiency could be attributed to the modifications and shrinkage of Ch/g-HNTs@ZnγM at higher temperatures, resulting in a lowering in the number of active sites. Furthermore, the adsorbed ions on the Ch/g-HNTs@ZnγM surface could detach them from the surface by increasing the temperature.

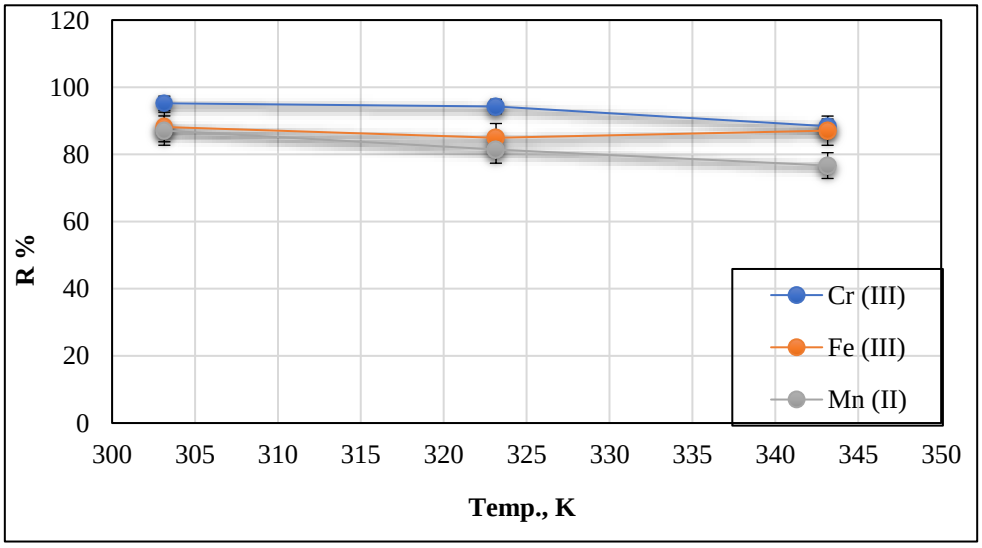

Figure 13. Effect of temperature on Cr (III), Fe (III), and Mn (II) removal at Conc. 20 mg/L and pH 9.

3.2.4. Effect of Adsorbent Dosage (Conc. 20 mg/L and pH 9)

The amount of adsorbent dosage used in metal ion removal is crucial as the adsorbent's equilibrium and the adsorbate are defined. The cost of adsorbent is also predicted. Figure 14 shows the experimental data regarding the adsorbent dosage effect on the % removal efficiency of Cr (III), Fe (III), and Mn (II) ions from their solution by Ch/g-HNTs@ZnγM while keeping all other parameters constant. It shows that with increasing the dose of adsorbent Ch/g-HNTs@ZnγM to 2 g, the removal efficiency % of Fe (III), Cr (III), and Mn (II) increased to be 96.9%, 97.5%, and 94.4%, respectively. The availability of more adsorbent surfaces for sorption may raise the metal ion removal rate at a high adsorbent dose. Previous studies have found similar behaviour caused by interactions between the metal ions and the adsorbent. The greater the region and the number of adsorption sites, the greater the overdose [42].

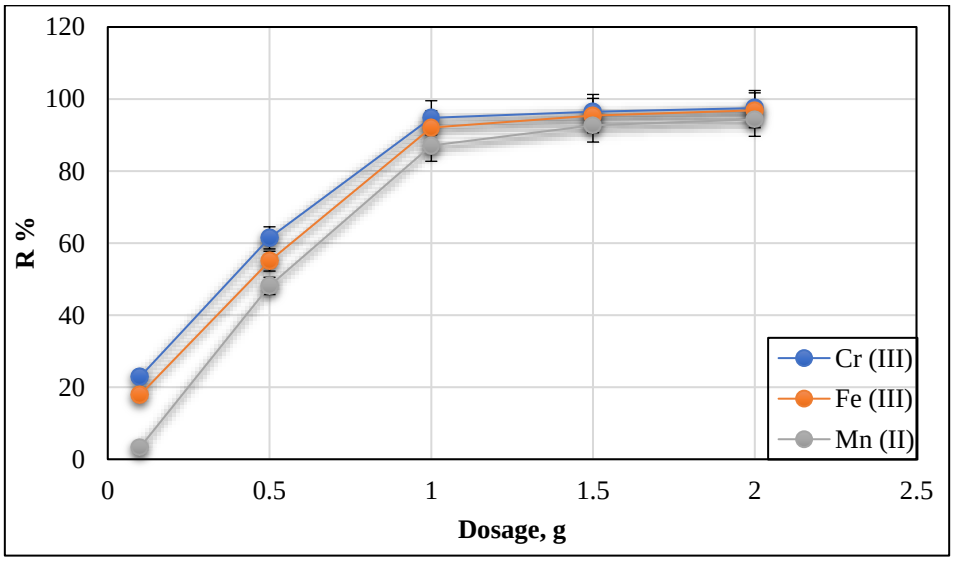

Figure 14. Adsorbent Ch/g-HNTs@ZnγM dosage versus removal % of Cr (III), Fe (III), and Mn (II).

3.2.5. Effect of Mixing Time

While holding all other parameters constant, the impact of mixing time on the adsorption removal of Cr (III), Fe (III), and Mn (II) ions onto Ch/g-HNTs@ZnγM was studied

in the range of 20, 40, 60, and 100 min. Figure 15 shows that the studied metals' removal efficiency was rapid between 20 and 60 min. By increasing time from 20 to 60 min, the removal efficiency % increases to 92%, 87%, and 94.8%, for Cr (III), Fe (III), and Mn (II) ions, respectively, with equilibrium being reached after 60 min for all the mentioned ions. The fast adsorption at the initial steps is regarded to the abundance of a large number of the surface-active sites on the adsorbent for the adsorption of the studied metals, which are used up over time and become saturated.

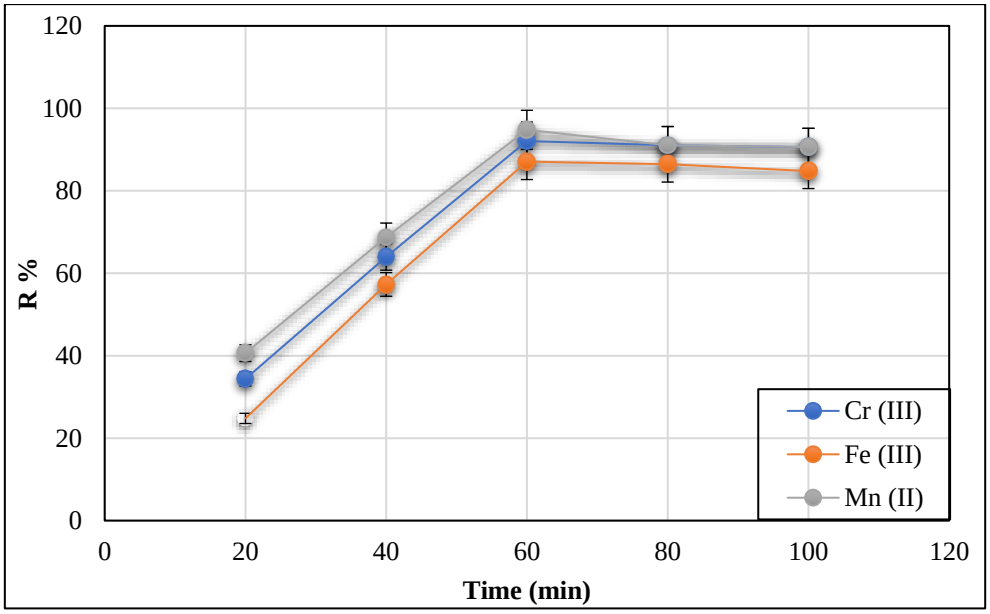

Figure 15. Effect of mixing time on Cr (III), Fe (III), and Mn (II) removal onto Ch/g-HNTs@ZnγM adsorbent.

3.2.6. Kinetics Study and Adsorption Modelling

This research included the two widely used kinetic models, pseudo-first-order and pseudo-second-order, to understand the adsorption process's kinetic mechanism (rate and type) [43].

The pseudo-first-order kinetic model is represented by Equation (2) [44].

$$\ln(q_e - q_t) = \ln q_e - k1.t/2.303 \quad (2)$$

The pseudo-second-order model is given by Equation (3) [44].

$$q_t/t = \frac{1}{k_2 q_e^2} + \frac{q_e}{t} \quad (3)$$

where, k_1 is the pseudo-first-order rate constant (min^{-1}) and k_2 ($g.mg^{-1}.min^{-1}$) is the pseudo-second-order rate constant. q_e (mg/g) and q_t refer, respectively, to the amount of metal ions adsorbed at equilibrium and at a time (t; min).

The linear curves of log ($q_e - q_t$) against time (min) and (q_e/t) against time (min) were plotted to calculate the constant rate values (k_1) and (k_2), respectively, as presented in Figures S1 and S2. The two models' corresponding parameters (R^2, K, and q_e (mg/g) of Cr (III), Fe (III), and Mn (II) ions adsorption on Ch/g-HNTs@ZnγM) are depicted in Table 3. The low K_1 value in the pseudo-first-order model indicates a slow adsorption rate, whereas the high K_2 value in the pseudo-second-order indicates an increase in the adsorption rates. The pseudo-second-order model regression coefficient ($R^2 \geq 0.96$) had a higher R^2 value for the metal ion adsorption kinetics than the pseudo-first-order model. As a result, the pseudo-second-order model can be better fitted for the kinetics of Cr (III), Fe (III), and Mn (II) ions adsorption (Figure S2).

Table 3. Constants of the pseudo-first-order and pseudo-second-order models.

Kinetic Order	Parameters	Metal Ions		
		Cr (III)	Fe (III)	Mn (II)
Pseudo-first-order	q_e (mg/g)	1.0234	1.0268	1.01547
	R^2	0.85433	0.29425	0.89897
	K_1 (min^{-1})	0.01478	0.0019	0.01023
Pseudo-second-order	q_e (mg/g)	2.4078	2.40781	2.63299
	R^2	0.98978	0.96695	0.9878
	K_2 (min^{-1})	1.626199	1.23978	0.70769

3.2.7. Adsorption Isotherm Modeling

Two adsorption isotherm (Langmuir and Freundlich) models of Cr (III), Fe (III), and Mn (II) ions adsorption onto Ch/g-HNTs@ZnγM tetra-nanocomposite are displayed in Figure S3. The mentioned two models are used to evaluate the affinity of sorbent and adsorbate and explain the adsorption mechanism. The Langmuir and Freundlich models can be presented by Equations (4) and (5) [45].

$$\frac{C_e}{q_e} = \frac{1}{K_L q_m} + \frac{C_e}{q_m} \tag{4}$$

$$\log q_e = \log K_f + (1/n) \log C_e \tag{5}$$

where q_e (mg/g) is the adsorption capacity at equilibrium, C_e is the metal ion concentration at equilibrium (mg/L), and q_m (mg/g) is the maximum monolayer adsorption capacity. K_L (L/mg) is the Langmuir constant, K_f (L/g) is the Freundlich constant, and n is the heterogeneity factor (index of the diversity, dimensionless).

The fundamental characteristic of the Langmuir isotherm model is represented in terms of separation factor (R_L), a dimensionless equilibrium parameter, described by Equation (6) [46].

$$R_L = 1/(1 + C_o \times K_l) \tag{6}$$

C_o (mg/L) is the amount of initial adsorbate and K_L (L/mg) is the separation factor. The parameter R_L is considered to be a more accurate adsorption indicator. The value of R_L suggested whether the adsorption is irreversible (R_L = 0), favorable (0 < R_L < 1), linear (R_L = 1), or unfavorable (R_L > 1).

By drawing the relation between log C_e and log q_e displayed in Figure S3, the Freundlich and exponent constants (K_f and n) are determined from the slope and intercept and of the straight lines. The estimated isotherm model constants and the related coefficients of correlation values are summarized in Table 4. Compared to the Langmuir isotherm model, the correlation coefficient "R^2" of the Freundlich isotherm was far from unity. The equilibrium data for Cr (III), Fe (III), and Mn (II) adsorption on Ch/g-HNTs@ZnγM have fitted the Langmuir model better than the Freundlich model, as shown in Figure S3. Langmuir model suggests that monolayer adsorption occurs due to a uniform distribution of active sites around the adsorbent surface.

3.2.8. Thermodynamic Adsorption Parameters

The thermodynamic parameters for adsorption and the values of K_{eq} (Langmuir constant; L/mg) at different temperatures (T; K) were processed according to the Van 't Hoff equation (Equation (7)) [47].

$$\ln K_{eq} = \frac{\Delta S^o}{R} + \frac{\Delta H^o}{RT} \tag{7}$$

where ΔH° (J/mol) and ΔS° (J/mol.K) are enthalpy and entropy changes, respectively.

Table 4. Adsorption isotherms constants for adsorption of Cr (III), Fe (III), and Mn (II) on (Ch/g-HNTs@ZnγM).

Model	Constants	Metal Ions		
		Cr (III)	**Fe (III)**	**Mn (II)**
Langmuir	q_m (mg/g)	0.893395	0.4467	0.23182
	K_L (L/mg)	0.231614	0.115807	0.107141
	R^2	0.999989	0.999989	0.999700
Freundlich	K_f	0.753768	0.351077	0.283438
	n	0.408312	0.41059	0.57226
	R^2	0.99261	0.98584	0.994095

Plotting ln K_{eq} against $1/T$ gives straight lines with slopes and intercepts equal to $\Delta H^\circ/R$ and $\Delta S^\circ/R$, respectively, from which enthalpy and entropy changes can be calculated as shown in Figure S4.

The Gibbs free (ΔG°; J/mol) of adsorption was calculated from the following relation [48] (Equation (8)):

$$\Delta G^o = \Delta H^o - T\Delta S^o \quad (8)$$

Table 5 shows the thermodynamic parameters of the reaction. For all metal ions, the entropy change is positive, indicating that the reaction is less random. In contrast, the enthalpy change and the ΔG° values are negative, indicating, respectively, that the process is exothermic and spontaneous with a favourable sorption process.

Table 5. Thermodynamic constants for the adsorption of Cr (III), Fe (III), and Mn (II) on the Ch/g-HNTs@ZnγM at various temperatures.

		Cr (III)	
T (K)	ΔH (J/mol)	ΔS (J/mol.K)	ΔG (J/mol)
303.15	−35,703.1	110.688	−69,258.1
323.15	−35,703.1	110.688	−71,471.9
343.15	−35,703.1	110.688	−73,685.6
		Fe (III)	
T (K)	ΔH (J/mol)	ΔS (J/mol.K)	ΔG (J/mol)
303.15	−30,960.4	99.57985	−61,148
323.15	−30,960.4	99.57985	−63,139.6
343.15	−30,960.4	99.57985	−65,131.2
		Mn (II)	
T (K)	ΔH (J/mol)	ΔS (J/mol.K)	ΔG (J/mol)
303.15	−43,996.5	135.2966	−85,011.6
323.15	−43,996.5	135.2966	−87,717.6
343.15	−43,996.5	135.2966	−90,423.5

4. Conclusions

In this paper, a novel Ch/g-HNTs@ZnγM magnetic quaternary nanocomposite was fabricated to remove the ions of Cr (III), Fe (III), and Mn (II)) from wastewater. Its characteristics were investigated utilizing FTIR, SEM, XRD, GPC, TGA, TEM, and surface zeta potential. Adsorption investigations were carried out at various conditions to determine their effects on the adsorption process and obtain the isotherms of reaction. The maximum removal % of Cr (III), Fe (III), and Mn (II) on the Ch/g-HNTs@ZnγM adsorbent reached 95.2%, 99.06%, and 87.1% at 40 mg/L of ion concentrations. The optimum removal for all studied metal ions was obtained at a pH of 9.0 and a contact time of 60 min, which were utilized for equilibrium removal. The thermodynamic study of adsorption was with negative values of ΔH°, ΔG°, and positive value of ΔS° indicates an exothermic, spontaneous, and chemical adsorption. For isotherm and kinetic modelling, the Langmuir isotherm and pseudo-second-order models were better fitted the experimental data.

Additionally, upon completion of the adsorption process in contaminated water, the magnetic properties of the synthesized tetra-nanocomposite represent an advantage for recovering its particles. Thus, the current study suggests the Ch/g-HNTs@ZnM tetra-nanocomposite as a highly efficient, promising, and green alternative source adsorbent in the wastewater treatment concept. Furthermore, by using Ch/g-HNTs@ZnγM for Cr (III), Fe (III), and Mn (II) adsorption, the environmental load, and effect of Ch/g-HNTs@ZnγM will be reduced, and so the impact of Ch/g-HNTs@ZnγM will via an environmentally friendly method.

Supplementary Materials: The following are available online at https://www.mdpi.com/article/10.3390/polym13162714/s1, Figure S1: Pseudo-first-order rate (60 mg/L) for Cr (III), Fe (III), and Mn (II) removal on/g-HNTs@ZnγM adsorbent, Figure S2: Pseudo second-order model (60 mg/L) for Cr (III), Fe (III), and Mn (II) removal on Ch/g-HNTs@ZnγM adsorbent, Figure S3: Langmuir model for (a) Cr (III), (b) Fe (III),and(c) Mn (II) and Freundlich model for (d) Cr (III), (e) Fe (III), and (f) Mn (II), Figure S4: Thermodynamic adsorption parameters for the adsorption of (a) Cr (III), (b) Fe (III), and (c) Mn (II) on Ch/g-HNTs@ZnγM.

Author Contributions: Conceptualization, A.H.R., I.A.A., and R.H.; methodology, A.H.R., I.A.A., and H.A.A.; software, A.E.S.; validation, H.A.A., A.E.S. and I.A.A.; formal analysis, I.A.A.; investigation, M.F.M.; resources, A.E.S. and I.A.A.; data curation, A.H.R. and I.A.A.; writing—original draft preparation, A.H.R. and I.A.A.; writing—review and editing, A.E.S., M.F.M., and R.H.; visualization, H.A.A.; supervision, R.H., and S.M.E.-B.; project administration, M.F.M.; funding acquisition, S.M.E.-B., A.H.R. and I.A.A. All authors have read and agreed to the published version of the manuscript.

Funding: This research was assisted funded by the Dean of Science and Research at King Khalid University via the General Research Project: Grant no. (R.G.P.1/355/42). The APC was funded by Taif University Researchers Supporting Project number (TURSP-2020/135), Taif University, Taif, Saudi Arabia.

Acknowledgments: The authors are grateful to the Dean of Science and Research at King Khalid University to make financial support available and thankful to the Egyptian Petroleum Research Institute for making the practical analysis. I would like to thank everyone in Water Desalination Group in the Egyptian Petroleum Research Institute [EPRI] for their efforts to produce that paper. The authors gratefully acknowledge financial support from Taif University Researchers Support-ing Project number (TURSP-2020/135), Taif University, Taif, Saudi Arabia.

Conflicts of Interest: The authors declare no conflict of interest.

Abbreviation

Ch	Chitosan
g-HNTs	grafted halloysite nanotubes
NaOH	sodium hydroxide
HCl	hydrochloric acid
$CaCO_3$	calcium carbonate
KOH	potassium hydroxide
DI	deionized water
SDS	an aqueous solution of sodium dodecyl sulfate
EDTA	ethylenediaminetetraacetic acid
$Fe(NO_3)_3$	ferric nitrate
$Zn(NO_3)_2$	zinc nitrate
$Zn\gamma Fe_3O_4$	Alpha iron zincate
FTIR	Fourier transform infrared
TGA	Thermogravimetric analysis
GPC	Gel permeation chromatography
XRD	X-ray diffraction
pHpzc	Point of zero charge
SEM	scanning electron microscope
TEM	Transmission electron microscopy

References

1. Singh, R.P.; Singh, P.; Araujo, A.S.F.; Hakimi Ibrahim, M.; Sulaiman, O. Management of urban solid waste: Vermicomposting a sustainable option. *Resour. Conserv. Recycl.* **2011**, *55*, 719–729. [CrossRef]
2. Agamuthu, P.; Fauziah, S. Waste management technologies in Malaysia: The future prospect. In Proceedings of the ICAST Future: An Integrated Approach towards Science and Technology for Sustainable Development, Pahang, Malaysia, 13–15 June 2008; pp. 1–3.
3. Ismail, M.; Akhtar, K.; Khan, M.; Kamal, T.; Khan, M.A.; M Asiri, A.; Seo, J.; Khan, S.B. Pollution, toxicity and carcinogenicity of organic dyes and their catalytic bio-remediation. *Curr. Pharm. Des.* **2019**, *25*, 3645–3663. [CrossRef] [PubMed]
4. Kumari, S.; Mishra, A. Heavy Metal Contamination. In *Soil Contamination*; IntechOpen: London, UK, 2021.
5. Jaishankar, M.; Tseten, T.; Anbalagan, N.; Mathew, B.B.; Beeregowda, K.N. Toxicity, mechanism and health effects of some heavy metals. *Interdiscip. Toxicol.* **2014**, *7*, 60. [CrossRef]
6. Blanusa, M.; Varnai, V.M.; Piasek, M.; Kostial, K. Chelators as antidotes of metal toxicity: Therapeutic and experimental aspects. *Curr. Med. Chem.* **2005**, *12*, 2771–2794. [CrossRef] [PubMed]
7. Sun, Y.; Wang, D.; Tsang, D.C.; Wang, L.; Ok, Y.S.; Feng, Y. A critical review of risks, characteristics, and treatment strategies for potentially toxic elements in wastewater from shale gas extraction. *Environ. Int.* **2019**, *125*, 452–469. [CrossRef]
8. Taleb, M.A.; Kumar, R.; Al-Rashdi, A.A.; Seliem, M.K.; Barakat, M. Fabrication of $SiO_2/CuFe_2O_4$/polyaniline composite: A highly efficient adsorbent for heavy metals removal from aquatic environment. *Arab. J. Chem.* **2020**, *13*, 7533–7543. [CrossRef]
9. Gunatilake, S. Methods of removing heavy metals from industrial wastewater. *Methods* **2015**, *1*, 14.
10. Azimi, A.; Azari, A.; Rezakazemi, M.; Ansarpour, M. Removal of heavy metals from industrial wastewaters: A review. *ChemBioEng Rev.* **2017**, *4*, 37–59. [CrossRef]
11. Kumar, R.; Sharma, R.K.; Singh, A.P. Cellulose based grafted biosorbents-Journey from lignocellulose biomass to toxic metal ions sorption applications-A review. *J. Mol. Liq.* **2017**, *232*, 62–93. [CrossRef]
12. Magdy, A.; Wassel, M.; Hosny, R.; Desouky, A.; Mahmod, A. Study the removal of cupper ions from textile effluent using cross linked chitosan. In Proceedings of the 8th International Conferences of Textile Research Division, Cairo, Egypt, 25–27 September 2017.
13. Burakov, A.; Burakova, I.; Galunin, E.; Kucherova, A. New carbon nanomaterials for water purification from heavy metals. In *Handbook of Ecomaterials*; Springer International Publishing: New York, NY, USA, 2018.
14. Perrich, J.R. *Activated Carbon Adsorption for Wastewater Treatment*; CRC Press: Boca Raton, FL, USA, 2018.
15. Anjum, M.; Miandad, R.; Waqas, M.; Gehany, F.; Barakat, M. Remediation of wastewater using various nano-materials. *Arab. J. Chem.* **2019**, *12*, 4897–4919. [CrossRef]
16. Yang, J.; Hou, B.; Wang, J.; Tian, B.; Bi, J.; Wang, N.; Li, X.; Huang, X. Nanomaterials for the removal of heavy metals from wastewater. *Nanomaterials* **2019**, *9*, 424. [CrossRef]
17. Gupta, K.; Joshi, P.; Gusain, R.; Khatri, O.P. Recent advances in adsorptive removal of heavy metal and metalloid ions by metal oxide-based nanomaterials. *Coord. Chem. Rev.* **2021**, *445*, 214100. [CrossRef]
18. Husnain, S.M.; Um, W.; Chang, Y.-S. Magnetite-based adsorbents for sequestration of radionuclides: A review. *RSC Adv.* **2018**, *8*, 2521–2540. [CrossRef]
19. Fathy, M.; Hosny, R.; Keshawy, M.; Gaffer, A. Green synthesis of graphene oxide from oil palm leaves as novel adsorbent for removal of Cu(II) ions from synthetic wastewater. *Graphene Technol.* **2019**, *4*, 33–40. [CrossRef]
20. Mishra, S.; Cheng, L.; Maiti, A. The utilization of agro-biomass/byproducts for effective bio-removal of dyes from dyeing wastewater: A comprehensive review. *J. Environ. Chem. Eng.* **2020**, *9*, 104901. [CrossRef]
21. Crini, G.; Lichtfouse, E.; Wilson, L.; Morin-Crini, N. Green adsorbents for pollutant removal. *Environ. Chem. A Sustain. World* **2018**, *18*, 23–71.
22. Hosny, R.; Abdel-Moghny, T.; Ramzi, M.; Desouky, S.; Shama, S. Preparation and Characterization of Natural Polymer for Treatment Oily Produced Water. *Int. J. Curr. Res.* **2014**, *6*, 5413–5418.
23. Luo, J.; Yu, D.; Hristovski, K.D.; Fu, K.; Shen, Y.; Westerhoff, P.; Crittenden, J.C. Critical Review of Advances in Engineering Nanomaterial Adsorbents for Metal Removal and Recovery from Water: Mechanism Identification and Engineering Design. *Environ. Sci. Technol.* **2021**, *55*, 4287–4304. [CrossRef] [PubMed]
24. Kanmani, P.; Aravind, J.; Kamaraj, M.; Sureshbabu, P.; Karthikeyan, S. Environmental applications of chitosan and cellulosic biopolymers: A comprehensive outlook. *Bioresour. Technol.* **2017**, *242*, 295–303. [CrossRef]
25. El Knidri, H.; Belaabed, R.; Addaou, A.; Laajeb, A.; Lahsini, A. Extraction, chemical modification and characterization of chitin and chitosan. *Int. J. Biol. Macromol.* **2018**, *120*, 1181–1189. [CrossRef]
26. Yu, D.; Wang, Y.; Wu, M.; Zhang, L.; Wang, L.; Ni, H. Surface functionalization of cellulose with hyperbranched polyamide for efficient adsorption of organic dyes and heavy metals. *J. Clean. Prod.* **2019**, *232*, 774–783. [CrossRef]
27. Ali, M.A.; Mubarak, M.F.; Keshawy, M.; Zayed, M.A.; Ataalla, M. Adsorption of Tartrazine anionic dye by novel fixed bed Core-Shell- polystyrene Divinylbenzene/Magnetite nanocomposite. *Alexandria Eng. J.* **2021**. [CrossRef]
28. Pighinelli, L.; Kucharska, M. Chitosan–hydroxyapatite composites. *Carbohydr. Polym.* **2013**, *93*, 256–262. [CrossRef]
29. Khan, F.S.A.; Mubarak, N.M.; Khalid, M.; Walvekar, R.; Abdullah, E.C.; Mazari, S.A.; Nizamuddin, S.; Karri, R.R. Magnetic nanoadsorbents' potential route for heavy metals removal—A review. *Environ. Sci. Pollut. Res.* **2020**, *27*, 24342–24356. [CrossRef] [PubMed]

30. Zhang, M.; Zhang, Z.; Peng, Y.; Feng, L.; Li, X.; Zhao, C.; Sarfaraz, K. Novel cationic polymer modified magnetic chitosan beads for efficient adsorption of heavy metals and dyes over a wide pH range. *Int. J. Biol. Macromol.* **2020**, *156*, 289–301. [CrossRef]
31. Gómez-Pastora, J.; Bringas, E.; Ortiz, I. Recent progress and future challenges on the use of high performance magnetic nano-adsorbents in environmental applications. *Chem. Eng. J.* **2014**, *256*, 187–204. [CrossRef]
32. Marotta, A.; Luzzi, E.; Salzano de Luna, M.; Aprea, P.; Ambrogi, V.; Filippone, G. Chitosan/zeolite composite aerogels for a fast and effective removal of both anionic and cationic dyes from water. *Polymers* **2021**, *13*, 1691. [CrossRef] [PubMed]
33. Mohapatra, M.; Anand, S. Synthesis and applications of nano-structured iron oxides/hydroxides–A review. *Int. J. Eng. Sci. Technol.* **2010**, *2*, 127–146. [CrossRef]
34. Luo, J.; Fu, K.; Yu, D.; Hristovski, K.D.; Westerhoff, P.; Crittenden, J.C. Review of advances in engineering nanomaterial adsorbents for metal removal and recovery from water: Synthesis and microstructure impacts. *ACS EST Eng.* **2021**, *1*, 623–661. [CrossRef]
35. Adegoke, H.I.; Adekola, F.A.; Fatoki, O.S.; Ximba, B.J. Sorptive Interaction of Oxyanions with Iron Oxides: A Review. *Pol. J. Environ. Stud.* **2013**, *22*, 7–24.
36. Hosny, R.; Fathy, M.; Abdelraheem, O.H.; Zayed, m.A. Utilization of Cross-Linked Chitosan/ACTF Biocomposite for Softening Hard Water: Optimization by Adsorption Modeling. *Egypt. J. Chem.* **2019**, *62*, 437–456. [CrossRef]
37. Saliu, T.; Oladoja, N. Assessing the suitability of solid aggregates for nutrient recovery from aqua systems. *J. Water Process. Eng.* **2020**, *33*, 101000. [CrossRef]
38. Toan, N.V. Production of Chitin and Chitosan from Partially Autolyzed Shrimp Shell Materials. *Open Biomater. J.* **2009**, *1*, 21–24. [CrossRef]
39. Zhang, Y.; Xue, C.; Xue, Y.; Gao, R.; Zhang, X. Determination of the degree of deacetylation of chitin and chitosan by X-ray powder diffraction. *J. Carbohydr. Res.* **2005**, *340*, 1914–1917. [CrossRef] [PubMed]
40. Rawtani, D. Future Aspects of Halloysite Nanotubes in Forensic Investigations. *J. Nanomed. Res.* **2017**, *6*. [CrossRef]
41. Vojoudi, H.; Badiei, A.; Bahar, S.; Ziarani, G.M.; Faridbod, F.; Ganjali, M.R. A new nano-sorbent for fast and efficient removal of heavy metals from aqueous solutions based on modification of magnetic mesoporous silica nanospheres. *J. Magn. Magn. Mater.* **2017**, *441*, 193–203. [CrossRef]
42. Chatterjee, S.; Adhya, M.; Guha, A.K.; Chatterjee, B.P. Chitosan from Mucorrouxii: Production and Physico-Chemical Characterization. *J. Process. Biochem.* **2005**, *40*, 395–400. [CrossRef]
43. Rawtani, D.; Pandey, G.; Tharmavaram, M.; Pathak, P.; Akkireddy, S.; Agrawal, Y.K. Development of a novel 'nanocarrier' system based on Halloysite Nanotubes to overcome the complexation of ciprofloxacin with iron: An in vitro approach. *Appl. Clay Sci.* **2017**, *150*, 293–302. [CrossRef]
44. El-Dakkony, S.R.; Mubarak, M.F.; Ali, H.R.; Gaffer, A.; Moustafa, Y.M.; Abdel-Rahman, A.-H. Composite thin-film membrane of an assembled activated carbon thin film with autoself-healing and high-efficiency water desalination. *Environ Dev Sustain* **2021**. [CrossRef]
45. Ahmed, H.A.; Mubarak, M.F. Adsorption of Cationic Dye Using A newly Synthesized CaNiFe2O4/Chitosan Magnetic Nanocomposite: Kinetic and Isotherm Studies. *J. Polym. Environ.* **2021**, *29*, 1835–1851. [CrossRef]
46. Athapaththu, S. A Comprehensive Study of Cd (II) Removal from Aqueous Solution via Adsorption and Solar Photocatalysis. Master Thesis, The University of Western, London, ON, Canada, 12 December 2013.
47. Ho, Y.-S. Review of second-order models for adsorption systems. *J. Hazard. Mater.* **2006**, *136*, 681–689. [CrossRef] [PubMed]
48. Simonin, J.-P. On the comparison of pseudo-first order and pseudo-second order rate laws in the modeling of adsorption kinetics. *Chem. Eng. J.* **2016**, *300*, 254–263. [CrossRef]